

LA-UR--02-5024

*Approved for public release;  
distribution is unlimited.*

*Title:* Initiation Experiments on PBXN-110

*Author(s):* L.M. Hull, J.R. Faulkner, G.T. Gray III, C.M. Cady  
W.R. Blumenthal

*Submitted to:* HQ AFSC/SEW



Los Alamos National Laboratory, an affirmative action/equal opportunity employer, is operated by the University of California for the U.S. Department of Energy under contract W-7405-ENG-36. By acceptance of this article, the publisher recognizes that the U.S. Government retains a nonexclusive, royalty-free license to publish or reproduce the published form of this contribution, or to allow others to do so, for U.S. Government purposes. Los Alamos National Laboratory requests that the publisher identify this article as work performed under the auspices of the U.S. Department of Energy. Los Alamos National Laboratory strongly supports academic freedom and a researcher's right to publish; as an institution, however, the Laboratory does not endorse the viewpoint of a publication or guarantee its technical correctness.

Form 836 (8/00)

# **Impact Initiation of PBXN-110: FY02 Progress**

**L.M. Hull, J.R. Faulkner, G.T. Gray III, C.M. Cady, W.R. Blumenthal**

## **Abstract**

This is a progress report for the work done on N110 response for the Air Force Safety Center. Various conditions of fragment impact on munitions admit the possibility of the appearance of at least two meso-/macroscale initiation mechanisms: shock and shear. In this report, we briefly review the mesoscale view and mention the microscale mechanisms that can deposit enough energy to cause thermal decomposition and, therefore, initiation of the explosive. Some attention is given to the relationship between the microscale and the mesoscale mechanisms, as this relationship is an active area of research in the Los Alamos National Laboratory (LANL) High Explosive Science program, primarily through information given on equations of state and constitutive behavior. Data relating to the use of a surrogate (mock) explosive are presented. The equation of state and the mechanical response for the explosive and the mock are provided.

Due to the complexity of the potential operational loading scenarios, empirical correlation techniques are often used both to describe impact initiation data and to estimate the results expected in other situations. We discuss one of these techniques and, within this context, present new data on PBXN-110 and PBX-9501. Parameter variations include the projectile velocity and confinement characteristics. The experimental context is derived from fragment impact of munitions. The configuration generates both shock and shear events.

## **Programmatic**

The Air Force Safety Center made \$100,000 available for this project in FY02. Roughly speaking, this covers the materials needed to buy the hardware for the experiments, and one staff member and two technicians for about six weeks. The most effective method for working at this level at LANL is to associate the work closely with other, similar work. The association used in this instance is with the LANL High Explosives (HE) Science program. The experimental techniques developed by the LANL program to study explosives of interest to DOE were applied to PBXN-110 using the Air Force funding. Additional supported efforts were the writing and delivery of a paper, and attendance at the Explosives Safety Seminar in August and at various meetings throughout the year. Both organizations benefit through the comparison of PBXN-110 to PBX-9501; however, the downside of the association approach to executing small programs is that the reporting and documentation requirements can become unmanageably large relative to the budget.

## **Long-term Objective**

The far-reaching goal is to be able to state, based on models, data, and theoretical understanding, the response of any explosive in any initial condition to any insult. The world is quite a long way from attaining this objective. There is reasonable depth of knowledge in the area of plane-shock initiation, which has been extended to two and three dimensions with some success, although the extensions are not fully validated. There is also a considerable body of work on thermal insults, but it is clear that the relevant event space has not been fully probed. The work conducted here addresses prompt shear-dominated effects generated by impact. Because we are attempting to isolate prompt effects (short dwell between impact and initiation), we have selected

an experimental configuration that only features impact surface confinement (there is neither lateral nor rear confinement). The information generated addresses a relatively unexplored region of the impact initiation event space.

## Introduction

Projectiles typically initiate explosive by prompt shock, with the shock collapsing pores, activating shear cracks, etc., to generate hot spots. Radial relief waves, caused by small projectile diameters, truncate the region of explosive that is shocked sufficiently to cause initiation, (Figure 1). As a result, projectile impact initiation threshold velocities are commonly much higher than the initiation threshold velocity for a semi-infinite plate impact due to the relief of the loading pulse.

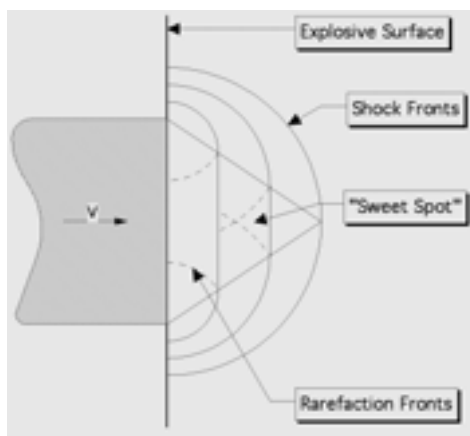


*Figure 1. The generally accepted idealized wave structures generated by projectile impact.*

If the explosive is covered, the cover plate enhances the radial relief effect, among other things such as impedance mismatch effects, and the initiation threshold velocity again increases. If the projectile velocity does not exceed the ballistic limit of the cover plate, initiation likelihood is suppressed. Projectile penetration causes a region of high shear around the perimeter and interaction with a rear cover at obliquity or a corner, due to deep penetration of a munition, and can also generate regions of high shear. It is known that shear can initiate explosive, and it is expected that elevated confinement pressure is a critical condition for shear initiation. When a projectile impacts a bare explosive, the region of high shear is relieved by the same radial waves that truncate the shocked region. Pre-plugging the impact location of the cover maintains the confinement while simultaneously permitting the peripheral shear effects. Such geometry is employed here to study shear initiation.

One objective of this work is to determine if shear initiation likelihood is significant in the geometry described above for PBXN-110 and PBX-9501. The experimental process entails the capture of data that show a reduced threshold (greater sensitivity) associated with the shear-initiation mechanism. As a matter of course, projectile impact shock initiation data are collected. Determined thresholds can contribute directly to safety assessments. If projectile impact could occur in a component containing geometric features that induce shear localization in the explosive, then the data collected can be used to separate dangerous impacts from inconsequential impacts, and thereby be used to validate empirical models. However, observed shear initiation events, in a well-controlled, fully specified geometry, provide for validation data for advanced computational techniques that should eventually include all physical effects leading to initiation. If the computational techniques can predict shear initiation from projectile impact and a spectrum of

other localization events, then we increase our confidence that the models will reasonably account for the existence of the shear initiation mechanism in more complex geometries that are experimentally inaccessible.

At the microscale, the individual crystals of explosive and intervening binder are considered. Micrographs of damaged explosives show that cracks can propagate directly through the explosive crystals, rather than following pathways defined by the binder or binder/energetic interfaces. Loads are transmitted through the contact of crystals and by the hydrostatic and deviatoric stresses in the binder. Relative motion can result in friction at an explosive-explosive interface (e.g., one HMX crystal sliding against another HMX crystal). Estimates of thermal deposition due to sliding friction indicate that this mechanism can indeed deposit enough energy to thermally decompose HMX, and is therefore a viable initiation mechanism. On the meso-/macroscale, the crystals and binder are thought of as a homogeneous material. Subgrid models can account for plastic deformation, cracking, and so on, of the homogeneous material. The physics for initiation are examined through such models.

## Material Descriptions

Fundamental to understanding any physical process are the descriptions of the materials involved under the appropriate conditions. Further, any computational model requires descriptions of the materials to close the set of equations and allow their solution. In “hydrocodes,” the deviatoric stresses are defined by subtracting one-third of the trace of the stress tensor from the full stress tensor, the assumed thermodynamic pressure. An equation of state is then used to describe the relationship between the pressure, volume, and energy, as is classically done for an ideal fluid. A constitutive model describes the relationship between the deviatoric stress and the displacements or strains (elastic/plastic). LANL has made measurements of the equations of state and has generated constitutive property data for PBXN-110 and PBX-9501 under the Joint Munitions Program<sup>1</sup>. In this effort, we have estimated the equation of state and generated constitutive property data for the mock N110. Thus, we have generated a first estimate of the information needed to understand the basic behavior of the material and to allow rudimentary computational modeling of the mock.

The mock’s equation of state has been estimated using the method of mixtures, a concise description of which is given by W. C. Davis in Zukas and Walters<sup>2</sup>. The two major assumptions are that the mixture is taken to be a completely homogeneous continuum, and that the volume of the mixture at any pressure is the mass-weighted sum of the volumes of the individual components. To apply this method, knowledge of the equations of state of the components is required. To form this equation of state, we generate the Hugoniot of the mixture and estimate of the Grüneisen gamma ( $\Gamma$ ) for the calculation of off-Hugoniot states. The generation of the mixture’s Hugoniot by the method of mixtures for two components is illustrated in Figure 2. The Hugoniots of the individual components are labeled H1 and H2, and the Hugoniot of the mixture is labeled M. The constant-volume offset from the Hugoniots is accomplished using the Grüneisen gamma. From the thermodynamic definitions,

$$\frac{\Gamma}{v} = \left( \frac{\partial p}{\partial E} \right)_v$$

and making the typical assumption that  $\Gamma/v = \text{constant} = \rho_0 \Gamma_0$  allows the estimation of off-Hugoniot states from

$$p(E, v) = p_H(v) + \rho_0 \Gamma_0 [E - E_H(v)]$$

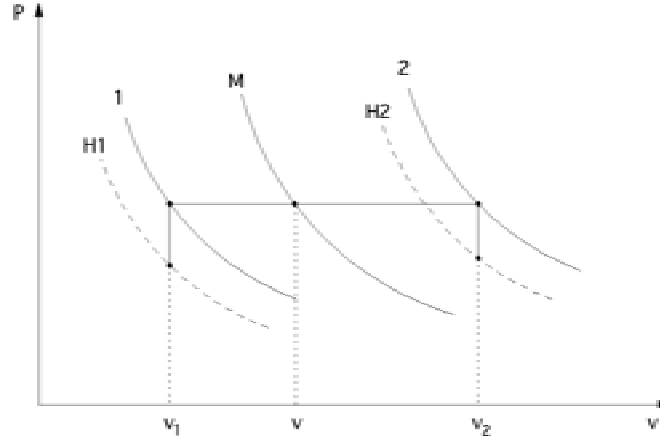


Figure 2. The method of mixtures for a two component system.

This approach is applied to each component. The pressure along the Hugoniot is acquired from the data. The continuum assumption forces the pressures of the components to be equal. These pressures are defined as lines 1 and 2 in Figure 2. The ideal mixing assumption defines the volume of the mixture. The last assumption used here is that there is no energy transfer between the components (a rapid process is envisioned) so that  $E_1 = E_2 = E_3$ . From this, the states along the Hugoniot for the mixture can be estimated as shown in the diagram.

This particular mock is 40% KCl, 40% “glass beads,” and 20% “binder” (an HTPB-based mixture). The nominal density of the mock is  $1.68\text{g/cm}^3$ . The salt has a density  $\rho_0 = 1.99\text{g/cm}^3$ , and at high pressure the Hugoniot is described by  $U = 2.150 + 1.54u$  mm/ $\mu\text{s}$ . For the glass beads, the data for fused quartz were used. At low pressure, the pressure is linear with the volume (elastic), but at higher pressure, the Hugoniot for quartz shows curvature, as expected. As a result, for the glass beads, a 9-term polynomial was fitted to the pressure-volume data covering the complete range for both high and low pressure regions. The binder is treated as a single entity with the Hugoniot taken from Berneker, APS 1996:  $\rho_0 = .897\text{g/cc}$ ,  $U = 1.63 + 2.24u$ . These data are claimed to be representative of N110 binder. The binder data are limited to pressures under 6 kbar. The Grüneisen coefficients for the salt, glass beads, and binder were estimated to be 1.6, 0.9, and 1.64, respectively. Figure3 shows the data and the curve fits used for each of the components. Note that the range of the data for the binder is indicated in Figure3, but there are actually very few data points. Nevertheless, to extend the mixture equation of state to a range useful for computational purposes, it was necessary to extrapolate the HTPB Hugoniot as shown in Figure3. The result of the mixture calculation, plotted in the pressure-particle velocity plane, is shown in Figure4.

The correspondence is reasonable over the range in data shown. The mixture range in particle velocity (and therefore pressure) is limited by the HTPB binder data set, which ends at  $0.6\text{mm}/\mu\text{s}$ . The range of the data provided for N110 in Reference 1 is limited to about  $0.45\text{mm}/\mu\text{s}$ . Other data in the literature generated at higher pressure on N110 need independent verification as they indicate complexity (possible phase transition) at particle velocities near  $0.5\text{mm}/\mu\text{s}$ . Further, due to the differences in slope, extrapolation to higher-pressure states appears to be a concern. Plotting the data in the shock velocity, the particle velocity plane allows fitting to a linear relationship, Figure 5.

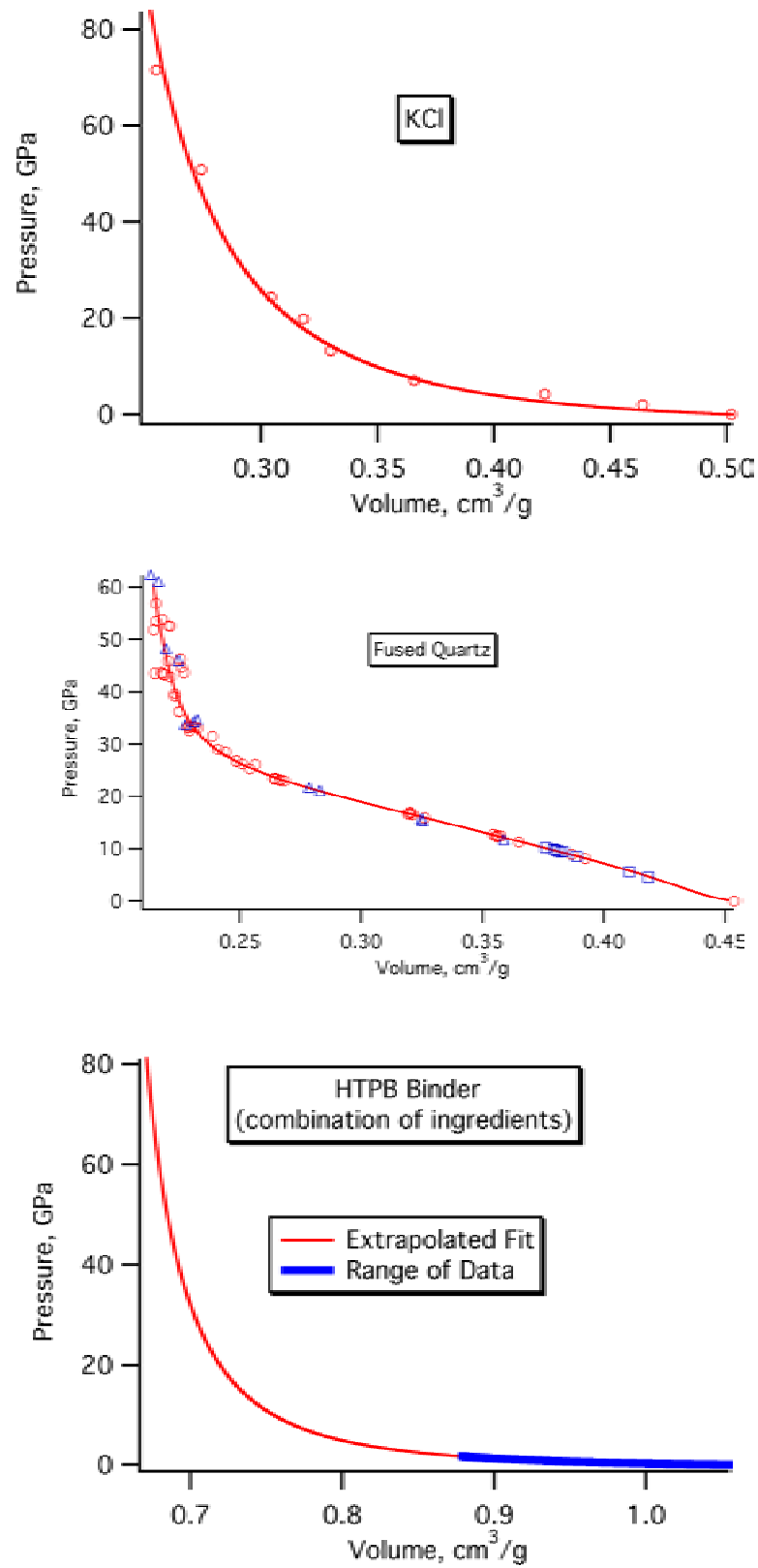


Figure 3. Hugoniot data for the components of the N110 mock mixture.

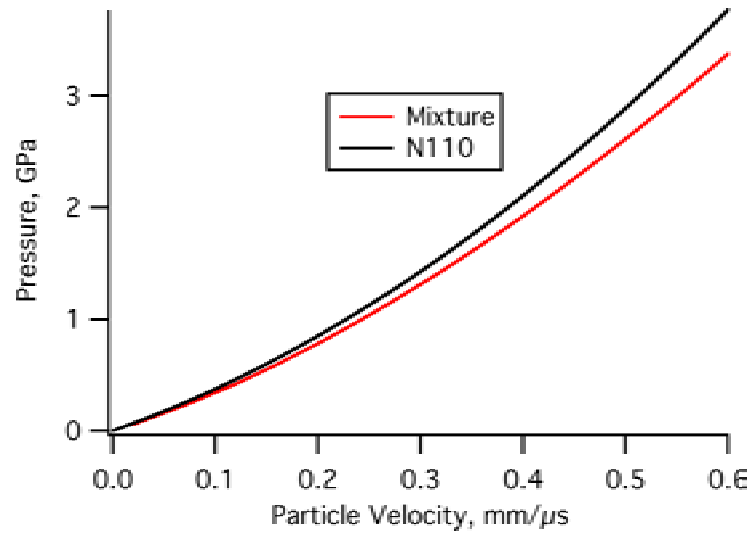


Figure 4. Calculated mock mixture Hugoniot compared to fitted N110 Hugoniot.

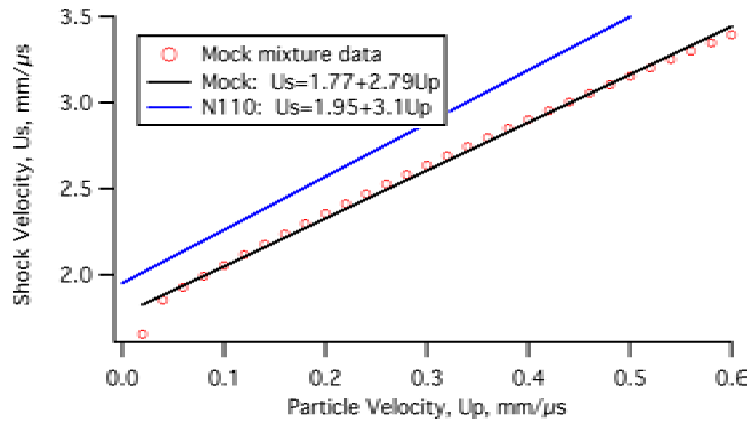


Figure 5. Comparison of linear shock velocity, particle velocity fits.

The linear fit ignores the slight curvature in the data, which is likely appropriate given the uncertainties. The linear fit to the N110 data of Reference 1 is provided for comparison. Although the mock is offset from the real explosive, it is not clear that this separation is greater than the uncertainty in the experimental data. The method of mixtures is known to work well for certain systems, particularly at high pressures. However, we don't have high-pressure data for all the materials involved. It is also known that some conditions of interest involve stress bridging between the hard materials and the slip (relative motion) between them. Both of these are violations of the assumptions of the mixture calculation. The result should be viewed as an approximation that allows consideration of the explosive as a single material that is valid over the range of the data.

The deviatoric material behavior of N110 and its mock have been measured using common mechanical property-testing techniques: low-rate compression testing machines and Hopkinson/Kolsky bar apparatus. Both sets of measurements were conducted by MST-8 personnel (Cady, Blumenthal, Gray) at LANL: the measurements on the mock were done specifically for this program. In these tests, the stress-strain behavior is captured as a function of strain rate and temperature. Data are shown in Figures 6 and 7.

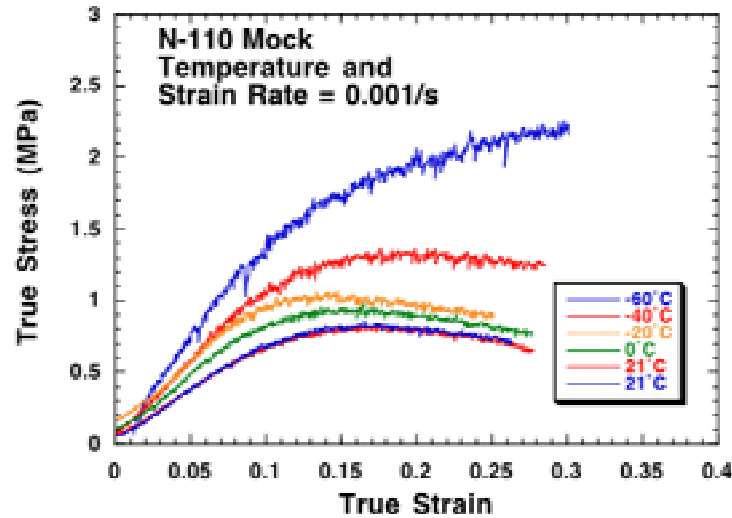


Figure 6. Quasi-static stress-strain response of N110 Mock at 0.001/s.

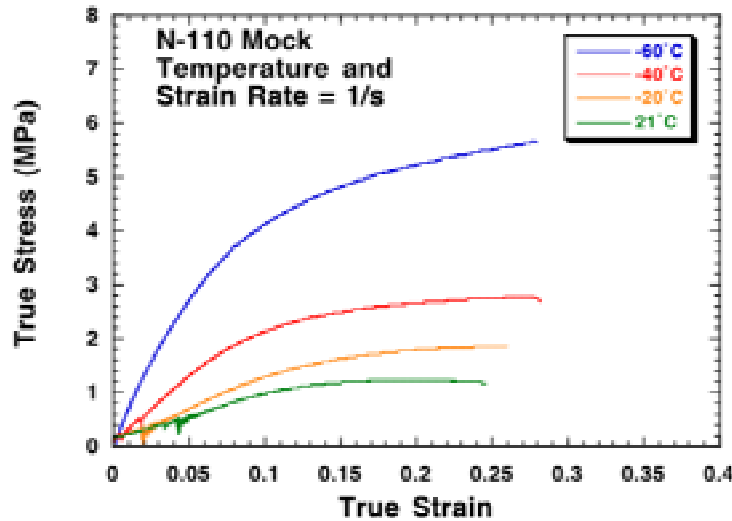


Figure 7. Quasi-static stress-strain response of N110 Mock at 1/s.

As can be seen, both the temperature and the strain rate have a pronounced influence on the mechanical behavior of the mock at low rate. At high (typical dynamic) rate, the effects are even more pronounced.

The response of the mock is compared to that of the actual N110 explosive in Figure 10. At low rate, the two materials display similar peak flow stresses but a different apparent loading modulus. A similar maximum flow stress during the quasi-static stress-strain testing for both PBXN-110 and mock energetic is consistent with comparable binder/solids decohesive responses and/or damage processes in both materials.

At high strain rate, the PBXN-110 displays a nearly 2x increase in flow stress for a given plastic strain, compared to the mock material. The significantly increased flow stress response for the PBXN-110 compared to the mock is consistent with a higher strain-rate sensitivity for HMX compared to the KCl and glass beads solid filling in the mock material.



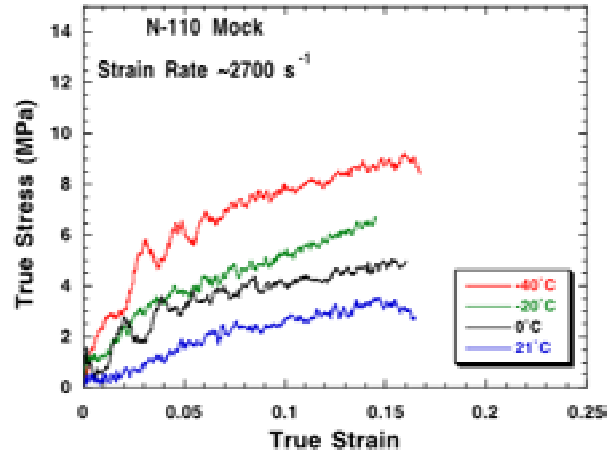


Figure 8. High strain rate response of N110 Mock at 0.001/s.

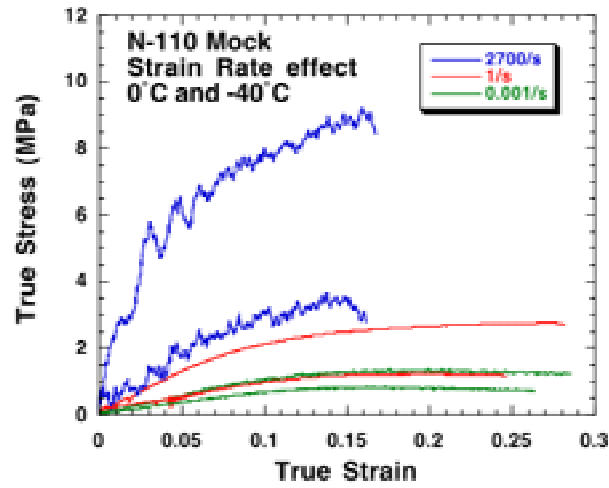


Figure 9. Influence of strain rate at  $0^\circ\text{C}$  and  $-40^\circ\text{C}$ .

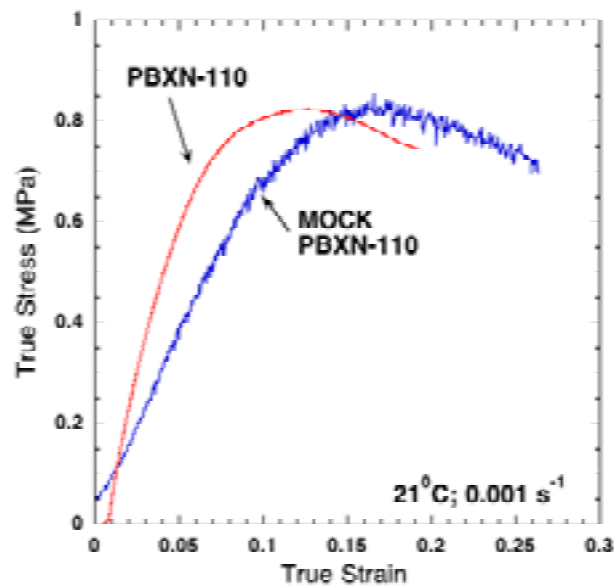


Figure 10. Comparison of quasi-static mechanical behavior between PBXN-110 and Mock.

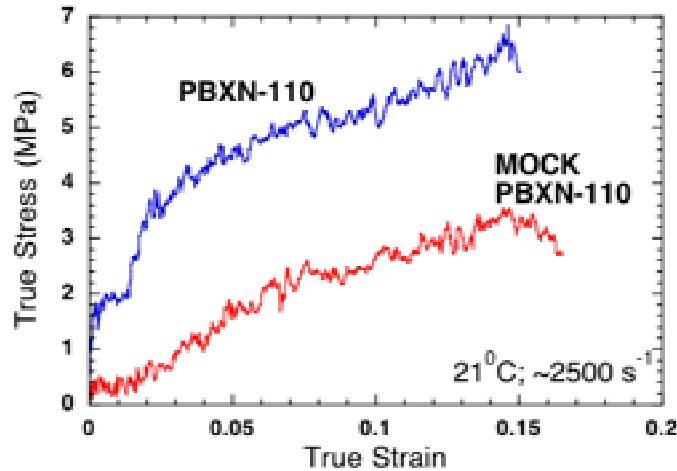


Figure 11. Comparison of high strain rate mechanical behavior between PBXN-110 and Mock.

The work done on the explosive is indicated by the area under the stress-strain curve. One significant consequence of this result is that, at high rate, more work will be deposited into the actual explosive. The mock is a good density match, an acceptable hydrodynamic match at low pressure, and an acceptable mechanical match at low strain rates to the explosive; however, it is not a good mechanical match at high strain rates, and the acceptability of the hydrodynamic match at high pressure is unknown.

### Impact Experiments

The experimental approach used here is that of a relatively simple projectile impact, shown in Figures 12 and 13.

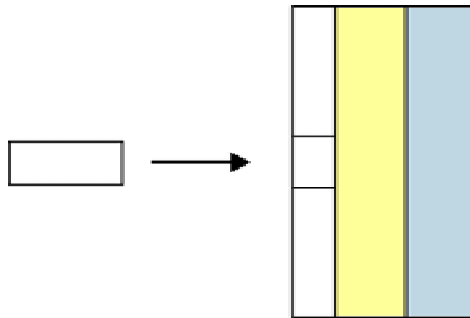


Figure 12. Projectile impact experiment geometry. The layers impacted are, from left to right: the cover plate (steel), the explosive (PBXN-110 or PBX-9501), and the rear “quencher plate” (transparent plastic).

The dimensions of the explosive are 75mm diameter and 10mm thick. The cover plate is 6.35mm thick. The central region of the cover plate shows a plugged portion. The diameter of this plug is nominally 10mm. However, the thickness of the plug is a variable of the experiment. This experiment differs from many other impact initiation experiments in that there is no radial confinement and, effectively, no rear confinement. The absence of confinement generally limits the studies to those effects that occur at a relatively early time. The optically clear rear cover plate admits the use of certain optical diagnostics. In particular, we have elected to record the shape of the detonation wave as it arrives at the rear surface. This geometry and the application of a smear camera are quite similar to the approach employed by Zxo<sup>3</sup>.

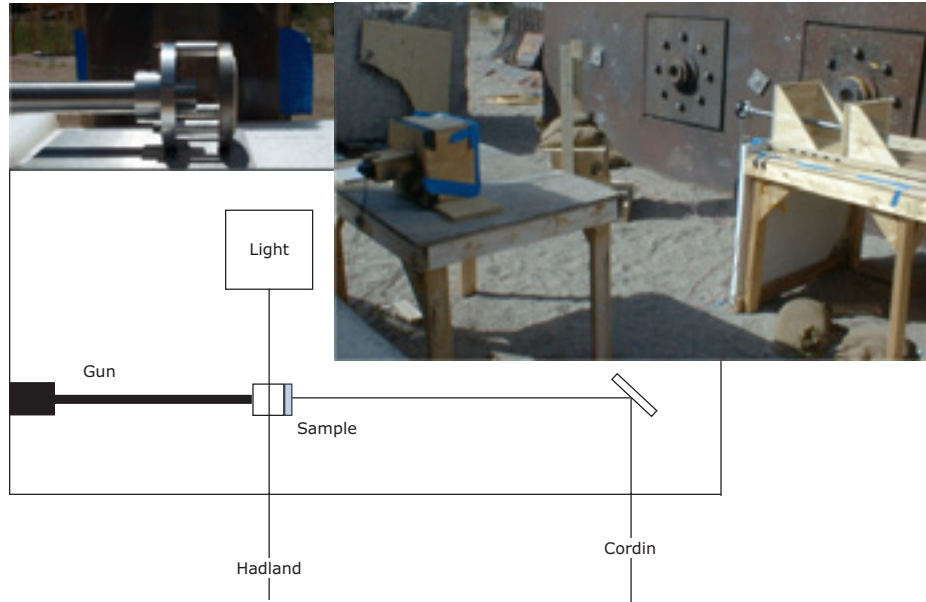


Figure 13. Layout of the experiment at the firing site. Upper left: explosive assembly. Upper right: firing site arrangement. Bottom: schematic of the firing site arrangement.

The projectile is a right circular cylinder with a length-to-diameter ratio ( $L/D$ ) of at least 1. The other details of the projectile and sabot design have varied. The projectile is fired from a 45-caliber smooth-bore research powder gun. Projectiles have been impacted against PBXN-110 and PBX-9501 at velocities ranging from 250m/s to 1800m/s. Because we are using a powder gun, the maximum velocity is just slightly above 2000m/s. The projectile attitude is controlled by use of a very short range, just a few centimeters. The projectile impact velocity and attitude are recorded with an electronic framing camera on each shot. Figure 14 shows a projectile/sabot configuration in free flight.

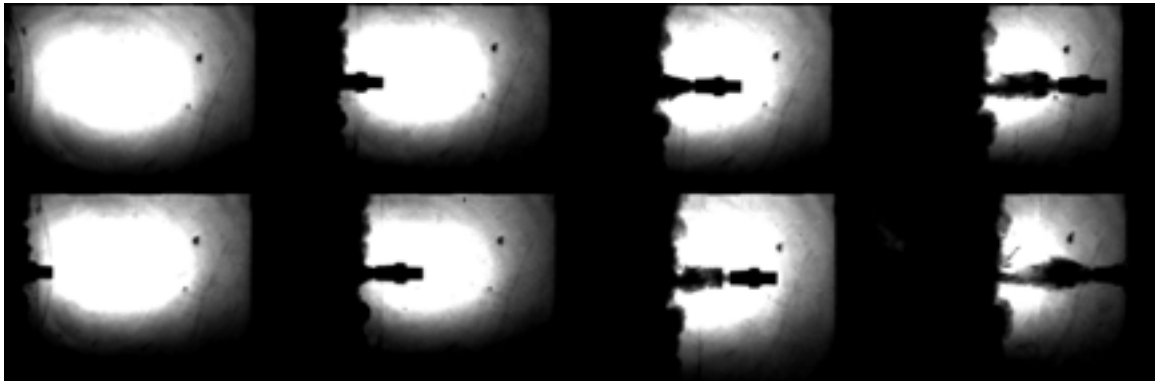


Figure 14. The 7mm-diameter projectile in free flight (H2670). The larger diameter band in the center is at the rear end of the projectile.

In a detonation initiated by shock, the wave arriving at the rear surface should arrive first at the centerline, whereas if initiation is by shear at the projectile periphery, first arrival will be offset from the centerline. An example of the framing camera and smear camera data generated in the shock initiation of bare PBX-9501 by a 7mm-diameter projectile moving at 1810m/s is given in Figures 15 and 16.

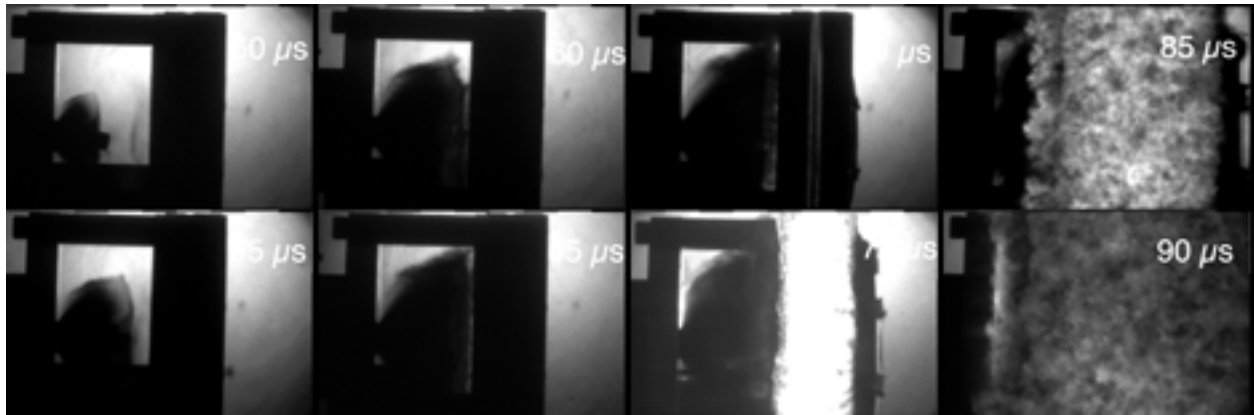


Figure 15. The framing camera data from shock initiation of PBX-9501, H2708.

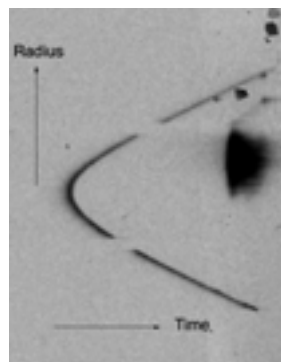


Figure 16. Smear camera data collected from the shock initiation of PBX-9501. Time increases from left to right, showing that the wave arrived first at the centerline.

## Results

There are many purely empirical and physical-approximation correlations for the description of initiation by projectile impact. We have chosen to use the Jacobs-Roslund empirical correlation because of its widespread use and the existence of constants for several explosives. PBXN-110 and PBX-9404 are included in the existing database. PBX-9404 is similar to PBX-9501, and can be used for comparisons. The PBXN-110 constants are based on two data points. A description of the Jacobs-Roslund correlation and a review of many initiation-influencing effects are given in Reference4, along with the constants used for the correlation in this paper. The correlation is based on the fact that the critical velocity can be determined by conducting a number of tests in which impact velocity and projectile diameter are the isolated parameters. The “go/no-go” line defined by the data can be viewed approximately as an iso-energy line. A combination of impact velocity and projectile diameter falling above the line indicates an initiation, and a combination falling below the line indicates no initiation. The energy required for initiation, corresponding to the implied energy deposition rate, is just satisfied along this line. However, the Jacobs-Roslund correlation contains no physics. It is simply a fit of the experimental data to a function. The trend observed in the data for a large variety of explosives is that the critical velocity is approximately proportional to the inverse of the square root of the projectile diameter. The effect of cover plates of various thicknesses and projectile shapes is handled with linear offsets to the bare explosive line. The Jacobs-Roslund correlation for PBXN-110 is given in

Figure 17. The data points are those collected in this study, whereas the solid lines are those defined by the constants in Reference4.

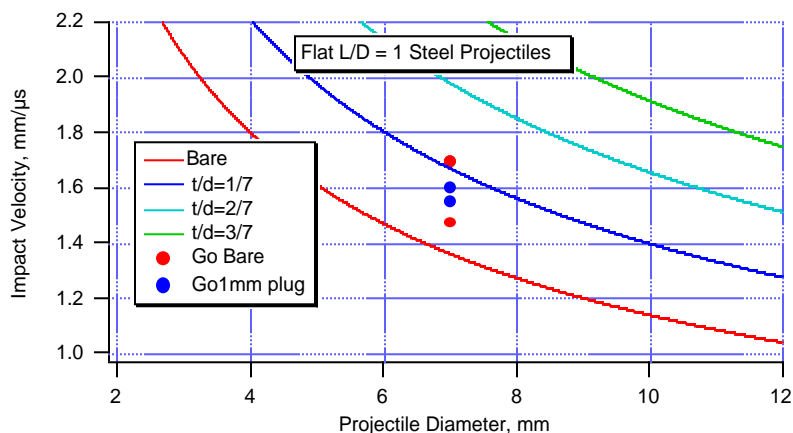


Figure 17. The Jacobs-Roslund correlation for PBXN-110.

All of the data points shown in Figure17 are listed as a “go”: “no-go” points exist at conditions not shown. Examination of the recovered shot assembly allows for a rudimentary classification of the severity of the induced reaction. In a “prompt detonation,” massive destruction of the assembly is achieved (Figure 18).



Figure 18. Prompt detonation destroys the explosive assembly, damages the muzzle of the gun, and drives the steel cover plate down the barrel and into the breech.

In a “violent reaction” event, it appears that only a small portion of the explosive energy is released on a time scale that will damage the apparatus. Thus, the recovered apparatus is damaged relative to a complete “no reaction” event, but far less damage is observed than in a prompt detonation. The damage generated in the intermediate case is compared to a pristine assembly and a “no reaction” event in Figures19a and 19b.

Although only a small amount of damage was inflicted on the unconfined assembly used here, it is expected that if such an event were to occur in a fully confined assembly, the result would be relatively energetic and violent. Therefore, this reaction was labeled “violent.” Observing Figure17, it is seen that at a 1mm plug (cover plate) thickness, the Jacobs-Roslund correlation predicts a non-initiation, or “no reaction,” event, whereas we have recorded a “violent reaction.” The correlation does not adequately represent the spectrum of results that are observed. This is not too surprising, considering that the correlation is not based on the physics of the event, and the data on which it is based are sparse.

The data collected here for PBX-9501 are compared to the Jacobs-Roslund correlation for PBX-9404 in Figure20. In the cases tested so far, the correlation appears to represent the data fairly well. The “go” shown in Figure 20 at  $t/d=3/7$  was a fully prompt detonation. The



Figure 19a. In the “no reaction” event, there is some damage to the area around the hole for the cover plug, but no dishing of the cover plate. In the “violent reaction” case, the front cover is dished in significantly.



Figure 19b. Side views.

“no-go” was the “no reaction” kind of event as defined in Figure 19. Thus, the different characteristics of the explosives are evident in the experimental data, but are not adequately described by the Jacobs-Roslund correlation.

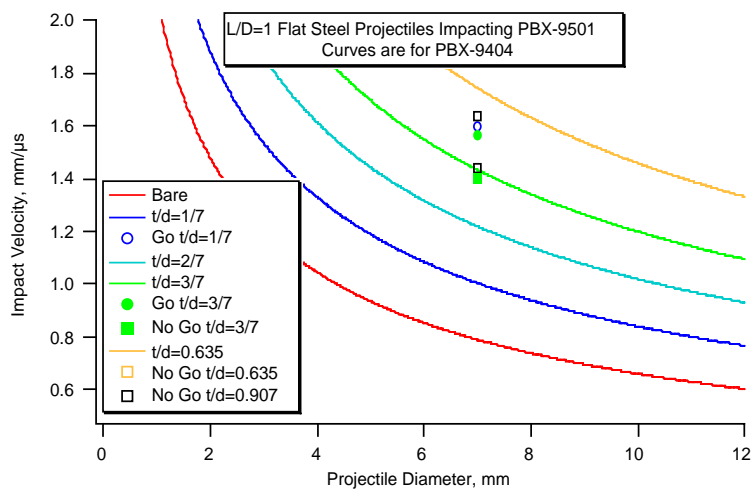


Figure 20. The PBX-9501 data of this study compared to the Jacobs-Roslund correlation for PBX-9504.

## Impact Calculations

The impact experiment described above, and its variations, have been calculated with the 2D Hydrocode MESA. This code is from the same “numerical family” of codes that includes CTH and Blanca. It is an Eulerian code: references on the specifics of the code are available on request. The setup for the baseline calculation is shown in Figure 21.

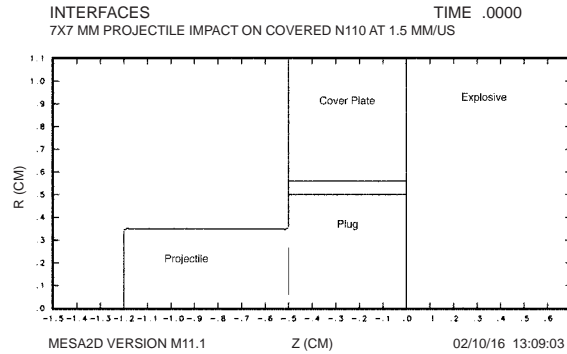


Figure 21. Initial configuration for the baseline impact experiment.

The narrow region between the plug and the cover is defined in the code as zero-strength steel. This is done to avoid a numerical artifact that effectively welds any two materials that have strength, together. In other words, the Eulerian code transmits stress across any two material interfaces as long as both materials have strength. Placing a layer of zero-strength material at the interface creates the effect of a zero-friction slide line. The projectile and the plug are defined initially in contact (and are therefore “welded together”), but the projectile has an initial velocity and the plug does not. In Figure 22, the configuration after an elapsed time of 10  $\mu$ s is shown. At this time, the projectile and plug have deformed, and are now in the process of penetrating the explosive.

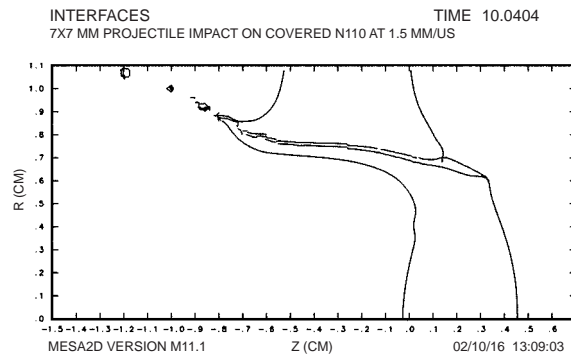


Figure 22. Configuration after an elapsed time of 10  $\mu$ s.

In Figure 23, the pressure distribution in the explosive is plotted. There are regions of elevated pressure (e.g., 10kbar) separated by regions of low pressure.

Figures 24a-24t show a time sequence with the axial pressure distribution over the interface plot. The first event is the impact of the projectile with the plug. This causes a shock wave to be driven through the plug and back through the projectile. These shock waves then interact with free or nearly free (the plug/explosive interface) surfaces. At the shock arrival at the free surfaces, the projectile and the plug are at high pressure and are compressed. Rarefactions are propagated



inward and interact with each other in the plug/projectile assembly, and a shock wave is driven into the explosive. The rarefactions create tensile waves that reflect from the free surfaces as compression waves. The right-going compression wave reaches the explosive/plug interface and drives another shock into the explosive. The sequence repeats, driving a shock into the explosive with each cycle of the “ringing” of the plug and projectile. Thus, the islands of high pressure observed in Figure 23 are caused by the ringing of the projectile after the impact.

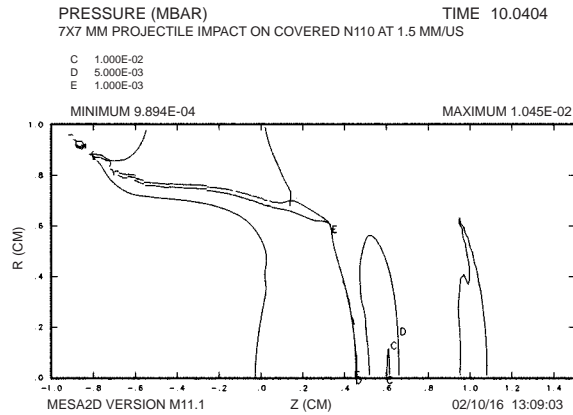


Figure 23. Pressure distribution in the explosive.

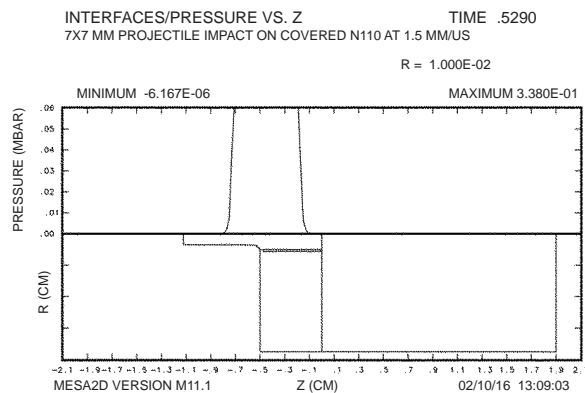


Figure 24a.

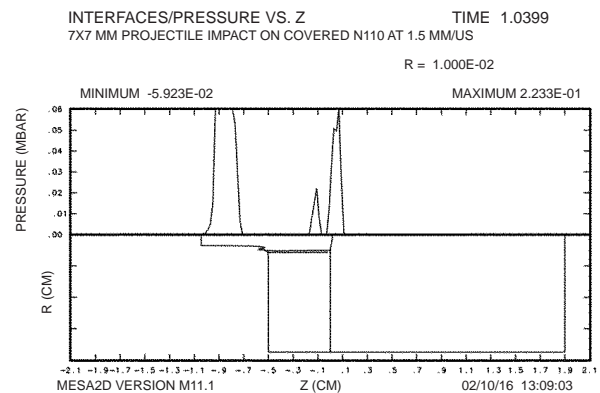


Figure 24b.

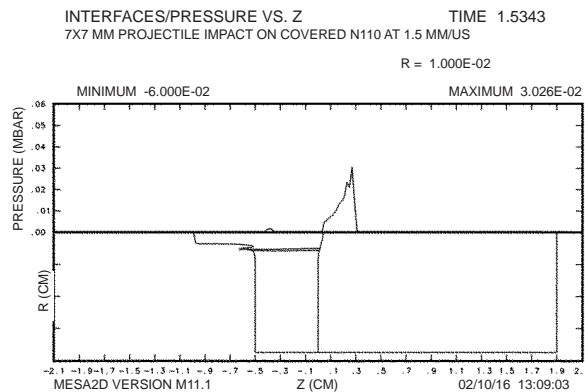


Figure 24c.

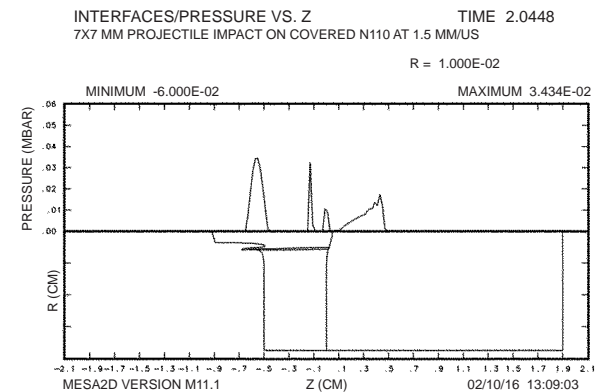


Figure 24d.



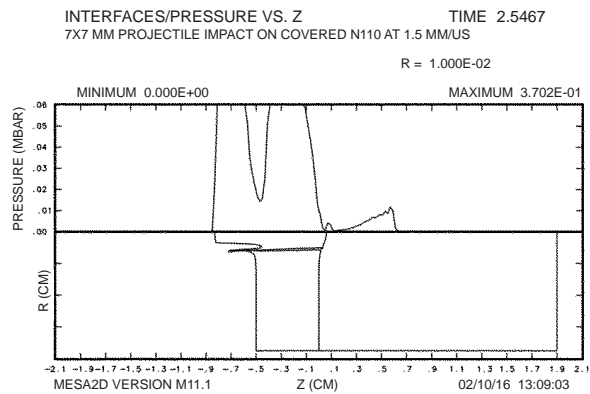


Figure 24e.

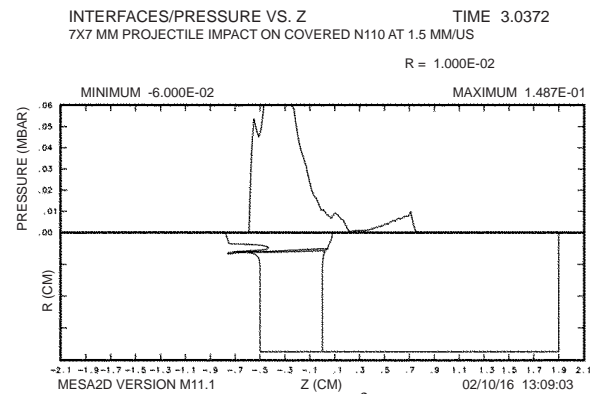


Figure 24f.

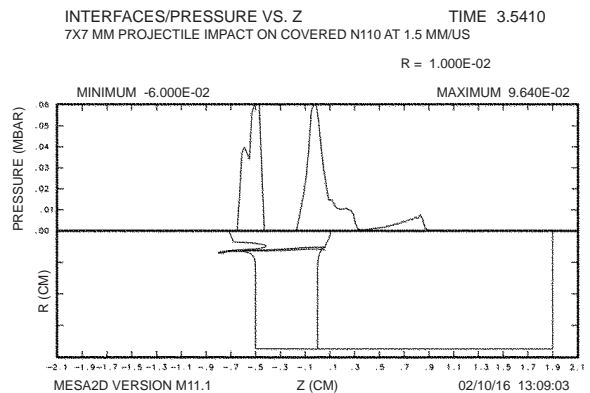


Figure 24g.

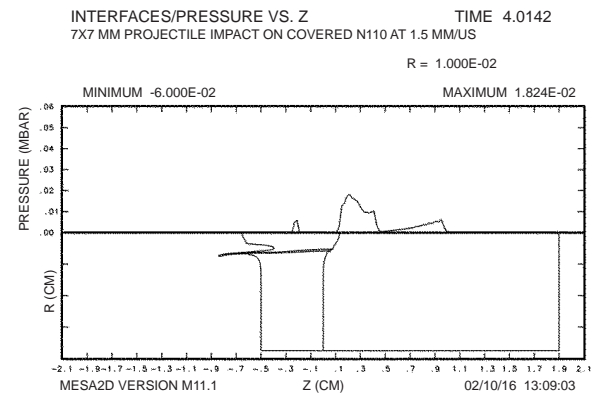


Figure 24h.

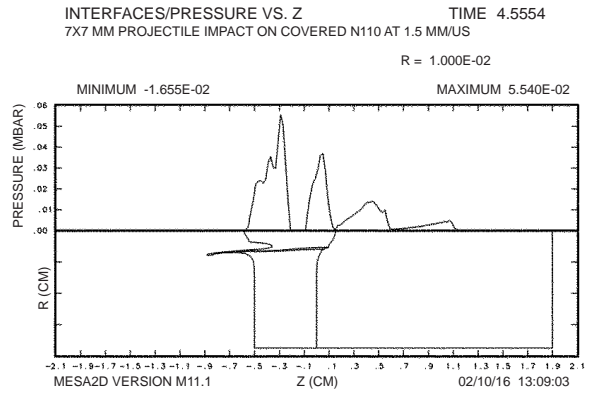


Figure 24i.

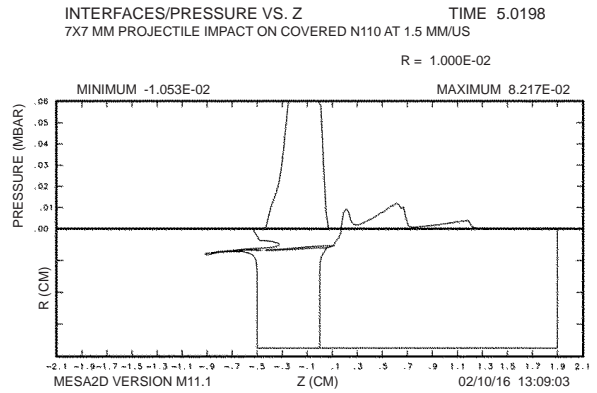


Figure 24j.

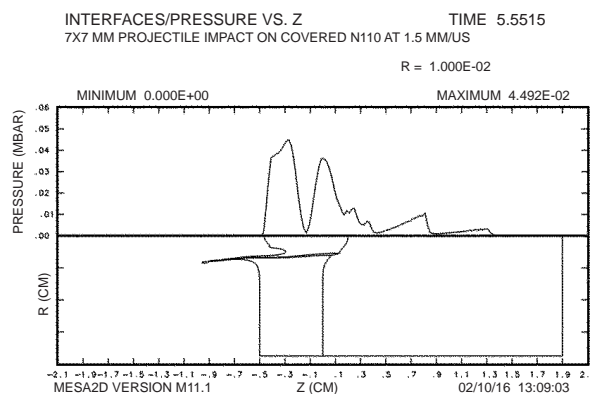


Figure 24k.

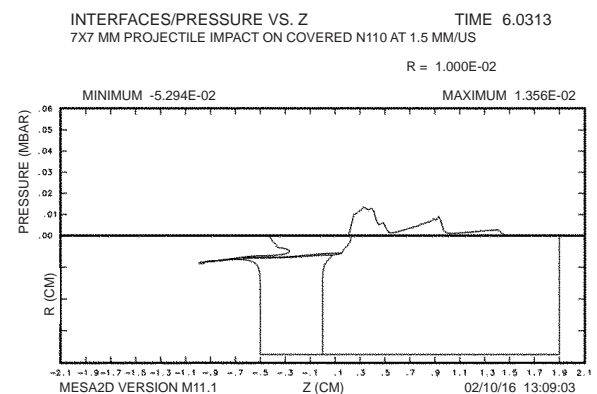


Figure 24l.

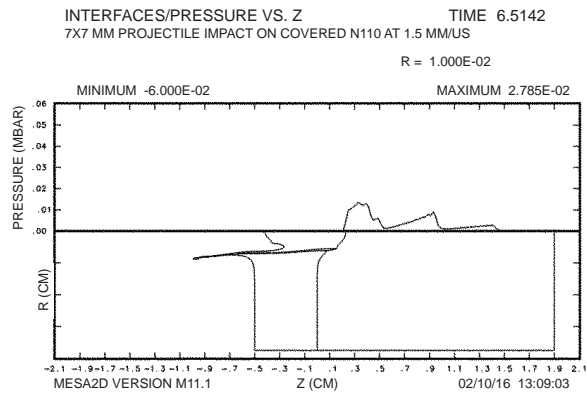


Figure 24m.

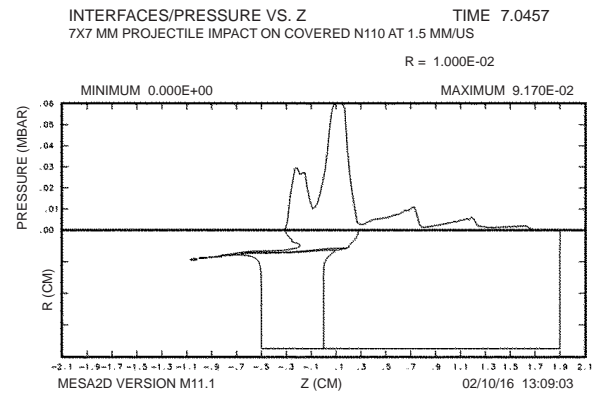


Figure 24n.

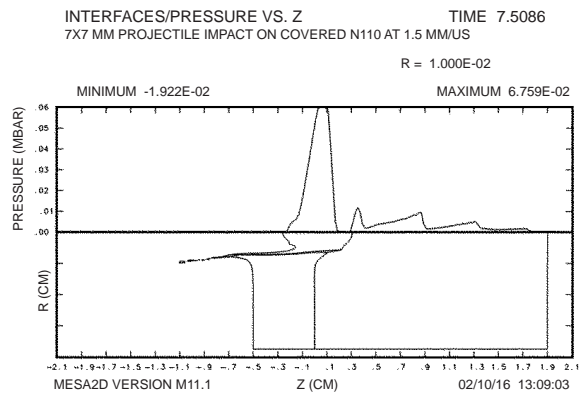


Figure 24o.

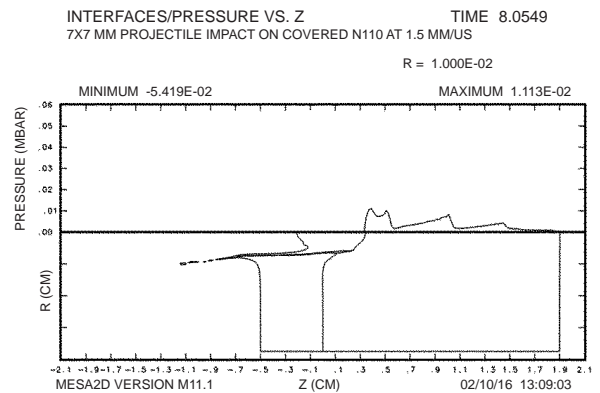


Figure 24p.

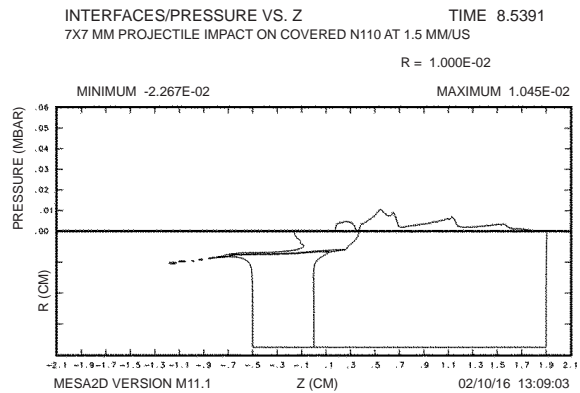


Figure 24q.

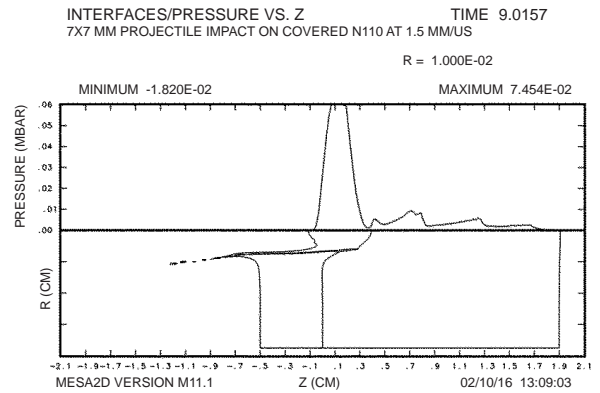


Figure 24r.

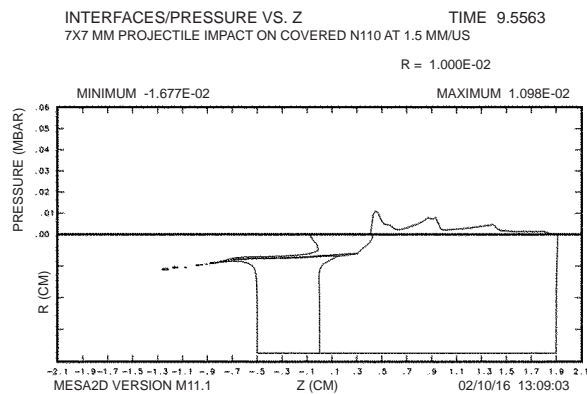


Figure 24s.

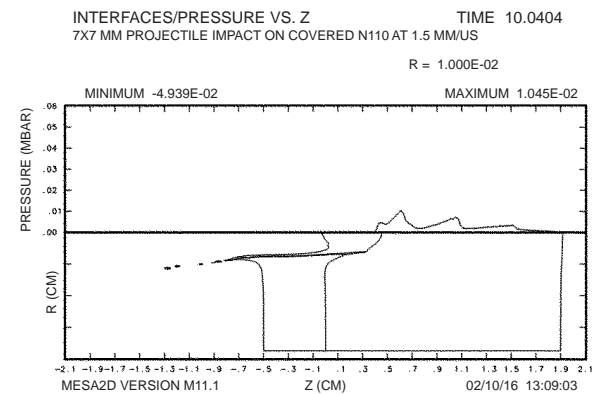


Figure 24t.

We are particularly interested in the possibility that the shearing process at the periphery of the plug may be capable of depositing sufficient energy to initiate the explosive. The explosive was modeled as a perfectly plastic material in these calculations, to allow the observation of some trends during energy deposition by shear. Figure 25 shows the distribution of the plastic work deposited into the explosive at 10  $\mu$ s.

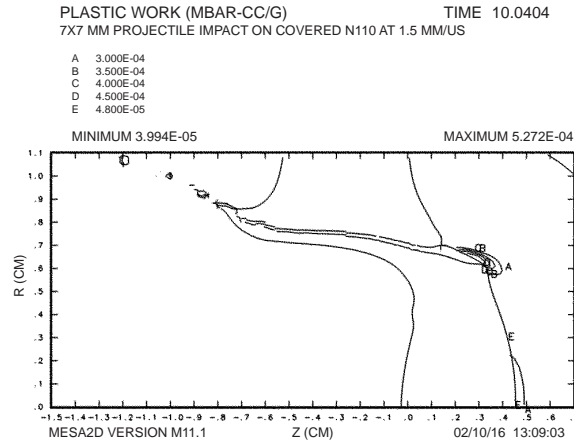


Figure 25. Distribution of the plastic work deposited into the explosive at 10  $\mu$ s.

Most of the plastic work is, as expected, deposited at the periphery of the plug. Physically on the microscale, the energy deposition mechanism involved in the shearing of the explosive is different than the plastic flow modeled here. Friction between explosive particles is one mechanism that is expected to be viable for shear initiation of explosive. To generate large amounts of friction, it is expected that the normal stresses (pressure) pushing the explosive grains into contact must be high. Figures 26a-26b show the pressure distribution in the axial direction, but in an offset position that intersects the periphery where the shearing process is concentrated. As can be seen in the figures, the ringing process at the periphery is similar to that on the axis, although the amplitude of the shocks is reduced. So, we see that the shear is concentrated around the periphery of the plug and that pressure pulses wash over this region.

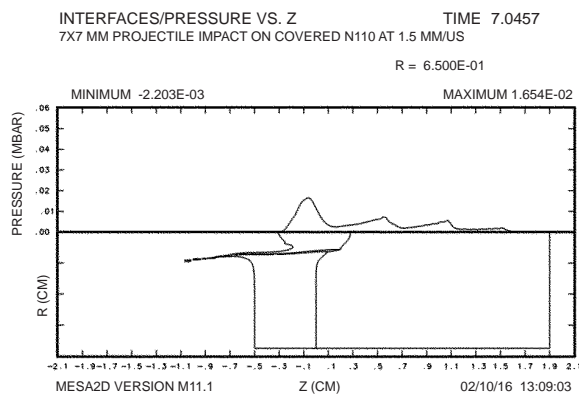


Figure 26a.

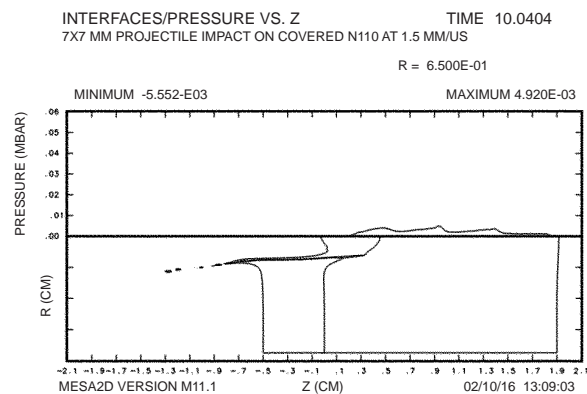


Figure 26b.

The pressure distribution in the explosive can be controlled to some degree by design of the experimental assembly. Figure 27a shows an example in which the explosive cover plate has been chamfered and the plug/projectile assembly modified by the insertion of an aluminum buffer between the plug and the projectile. In Figure 27b, it is seen that the plug/projectile assembly is expanded radially and is about to impact the chamfered cover plate. The pressure

distribution up to this time ( $4 \mu\text{s}$ ), Figure 27c, is quite similar to the baseline case. After impact ( $5 \mu\text{s}$ ), Figure 27d, a significant high-pressure region has developed around the periphery of the plug.

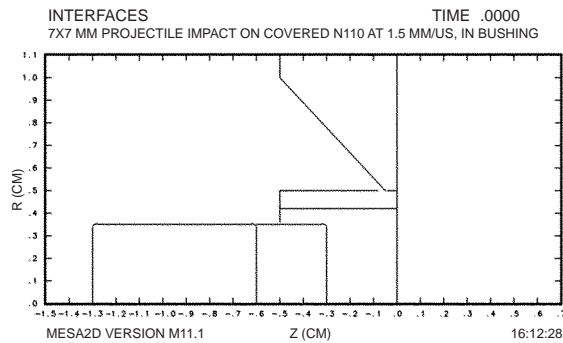


Figure 27a.

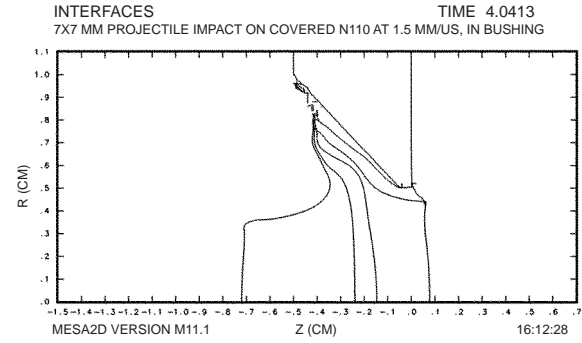


Figure 27b.

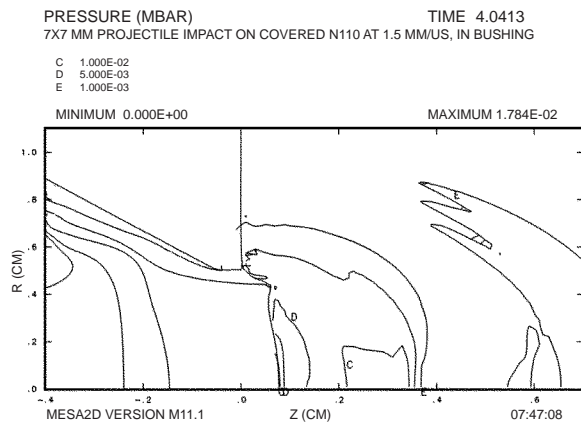


Figure 27c.

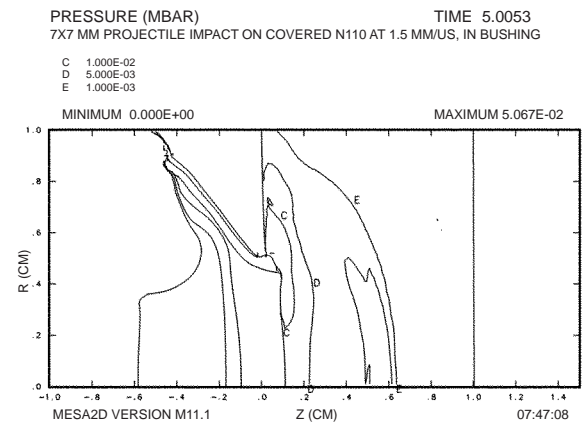


Figure 27d.

## Computational Tools

As discussed in the results above, strictly empirical correlations will not adequately represent the spectrum of observed events; however, there are a number of semi-physical models available, and there are a number of models designed for use in hydrocodes. The hydrocode models have the greatest potential for capturing the correct physics because all of the variables (kinematic and state) are, or can be, computed and available to the models. The semi-physical approach is typically more limited, but can also be useful. For instance, the divergence of the shock structure can be approximated by a few assumptions, and can lead to improved rendering of the shock initiation threshold. Non-shock initiation models must strive to include the appropriate effects, such as shear around the projectile periphery, crack conditions, and so on. A useful review of some of these models is given in Reference 5.

LANL is developing and improving many advanced computational models and techniques for application to problems, such as the experiments described here and their safety-specific counterparts. Comparison to the data generated in this study is expected to commence in the near future. As an illustration of the capability of one such approach, statistical crack mechanics (SCRAM), as applied to a ceramic composite material is given here. As extracted directly from Reference 6, Figure 28 shows the computed results of an impact of a rod against an idealized ceramic assembly. The damage inflicted on the ceramic by the rod is indicated by the generation

of porosity. As can be seen in Figure 28, the maximum damage occurs around the periphery of the projectile. In this calculation, the impact velocity was below the ballistic limit of the cover around the ceramic. Nevertheless, this computation clearly shows the ability to describe mechanical effects due to shear. Furthermore, because the cracks have been modeled, thermal deposition due to friction in the cracks can also be described. This kind of modeling is being developed and applied to explosives by the authors of Reference 6.

Figure 28 is actually two charts, earlier and later.

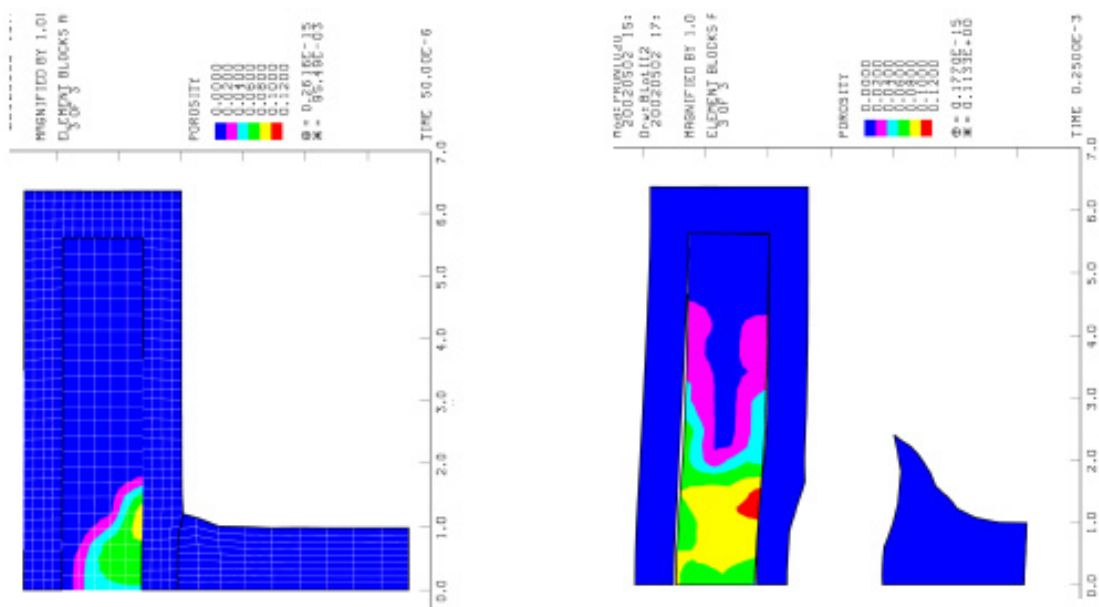


Figure 28. Impact of a rod against a ceramic assembly, as calculated with SCRAM.  
At the earlier time, the rod is in contact with the assembly. At the later time, the rod has rebounded.  
Note that the maximum porosity (damage) occurs around the periphery of the rod.

## Conclusions

The work presented here is in progress. However, it is already clear that simple correlation techniques will not be adequate to describe the response of PBXN-110 because of the appearance of a spectrum of reaction behavior. On the other hand, PBX-9501 has shown a much more binary behavior. The less sensitive formulation of PBXN-110 apparently facilitates the appearance of intermediate responses, and the Jacobs-Roslund correlation may not capture this behavior in a conservative way. As a result, it is not appropriate to base safety decisions on the Jacobs-Roslund correlation alone, but rather munitions must be tested against specific threats over a variety of interaction scenarios (e.g., impact obliquity, fragment orientation).

Hydrocode models hold out the possibility of rendering the physics of any particular defined interaction, as long as the explosives and metals are characterized, the threat is characterized, and the modeling is sufficiently validated. It is the authors' belief that the explosives community is still unable to offer a code that is fully validated for every conceivable problem. Review of Reference 5 reveals that non-shock initiation is the least well-understood class of phenomena relating to fragment impact. Still, it is possible to experimentally validate models of the physical processes that handle certain subsets, such as shock and shear initiation. Then, the hydrocode models can be exercised to contribute to safety analysis.

## Recommendations

- 1) Critical decisions should not be based on experimental results involving the mock if the experiments involve shock pressures in excess of 6 kbar. The radical change in slope of N110's Hugoniot observed in the NSW C data<sup>4</sup> is unexplained. If the data are good, then some unidentified phenomenon (e.g., a phase transition, cracking, reaction) is responsible. It is not likely that such phenomena would be well modeled by the mock.
- 2) Critical decisions should not be based on experimental results involving the mock if the experiments involve the mechanical properties at high strain rates. The energy deposited in the explosive could be as much as twice that deposited in the mock, and the motion of the mock, due to the lower strength, could be radically different in the explosive.
- 3) Critical decisions should not be based strictly on the Jacobs-Roslund correlation. Conditions in which the correlation is not conservative have already been observed. Such correlations can be used as a guide for more complete studies.
- 4) More sensitive data should be developed, refined, and corroborated to contribute to the assessment of the complex phenomenology involved, through the use of ever-more sophisticated codes.
- 5) The influence of geometric features (e.g., grooves) at explosive/metal interfaces upon the initiation of explosives should be investigated.

## References

1. 2002 Annual Report for the Joint DoD/DOE Munitions Technology Development Program, as yet unpublished.
2. Zukas, J. A. and Walters, W. P., Ed. *Explosive Effects and Applications*, Springer, 1997.
3. Shouqi, Zhang, et. al. "An Investigation of Projectile Impact Initiation Mechanism of Detonation in Explosive Charges Covered with a Thick Steel Plate," 15th International Symposium on Ballistics, Jerusalem, Israel, 21 May 1995.
4. Liddiard, T. P. and Roslund, L. A. "Projectile/Fragment Impact Sensitivity of Explosives," NSWC TR 89-184, June 1993.
5. Fisher, M., and Peugeot, F., "Fragment Impact Testing: NIMIC's Review and Proposal," NIMIC L-86, 30 April, 2002.
6. Zuo, Q. H., Dienes, J. K., Middleditch, J., and Meyer, H. W. Jr., "Modeling The Ballistic Performance Of Ceramic Armor Via Statistical Crack Mechanics," 5th Joint Classified Bombs/Warheads & Ballistics Symposium, Colorado Springs, Colorado, 18-20 June 2002.
7. Bourne, N.K., and Field, J.E., "Explosive Ignition by the Collapse of Cavities," Proc. Royal Society A, Vol. 455 (1999), pp. 2411-2426.



## List of Figures.

Figure 1. The generally accepted idealized wave structures generated by projectile impact. ....	2
Figure 2. The method of mixtures for a two component system. ....	4
Figure 3. Hugoniot data for the components of the N110 mock mixture. ....	5
Figure 4. Calculated mock mixture Hugoniot compared to fitted N110 Hugoniot. ....	6
Figure 5. Comparison of linear shock velocity, particle velocity fits. ....	6
Figure 6. Quasi-static stress-strain response of N110 Mock at 0.001/s. ....	7
Figure 7. Quasi-static stress-strain response of N110 Mock at 1/s. ....	7
Figure 8. High strain rate response of N110 Mock at 0.001/s. ....	8
Figure 9. Influence of strain rate at 0° C and -40° C. ....	8
Figure 10. Comparison of quasi-static mechanical behavior between PBXN-110 and Mock. ....	8
Figure 11. Comparison of high strain rate mechanical behavior between PBXN-110 and Mock. ....	9
Figure 12. Projectile impact experiment geometry. ....	9
Figure 13. Layout of the experiment at the firing site. ....	10
Figure 14. The 7mm-diameter projectile in free flight (H2670). ....	10
Figure 15. The framing camera data from shock initiation of PBX-9501, H2708. ....	11
Figure 16. Smear camera data collected from the shock initiation of PBX-9501. ....	11
Figure 17. The Jacobs-Roslund correlation for PBXN-110. ....	12
Figure 18. Prompt detonation destroys the explosive assembly, damages the muzzle of the gun, and drives the steel cover plate down the barrel and into the breech. ....	12
Figure 19a. In the “no reaction” event, there is some damage to the area around the hole for the cover plug, but no dishing of the cover plate. In the “violent reaction” case, the front cover is dished in significantly. ....	13
Figure 19b. Side views. ....	13
Figure 20. The PBX-9501 data of this study compared to the Jacobs-Roslund correlation for PBX-9504. ....	13
Figure 21. Initial configuration for the baseline impact experiment. ....	14
Figure 22. Configuration after an elapsed time of 10 $\mu$ s. ....	14
Figure 23. Pressure distribution in the explosive. ....	15
Figures 24a-t. Time sequence with the axial pressure distribution over the interface plot. ....	15-17
Figure 25. Distribution of the plastic work deposited into the explosive at 10 $\mu$ s. ....	18
Figures 26a-b. Pressure distribution in the axial direction, but in an offset position. ....	18
Figures 27a-d. The explosive cover plate has been chamfered and the plug/projectile assembly modified by the insertion of an aluminum buffer. ....	19
Figure 28. Impact of a rod against a ceramic assembly, as calculated with SCRAM. ....	20